

## Article

# Prediction of Tribological Properties of Alumina-Coated, Silver-Reinforced Copper Nanocomposites Using Long Short-Term Model Combined with Golden Jackal Optimization

Ismail R. Najjar <sup>1</sup>, Ayman M. Sadoun <sup>1</sup>, Adel Fathy <sup>2,3</sup> , Ahmed W. Abdallah <sup>2</sup>, Mohamed Abd Elaziz <sup>4,5,6</sup>  and Marwa Elmahdy <sup>3,\*</sup>

- <sup>1</sup> Mechanical Engineering Department, Faculty of Engineering, King Abdulaziz University, Jeddah P.O. Box 80204, Saudi Arabia  
<sup>2</sup> Department of Mechanical Design and Production Engineering, Faculty of Engineering, Zagazig University, Zagazig 44519, Egypt  
<sup>3</sup> Mechanical Department, Higher Technological Institute, Tenth of Ramadan City 44629, Egypt  
<sup>4</sup> Faculty of Computer Science & Engineering, Galala University, Suze 43511, Egypt  
<sup>5</sup> Artificial Intelligence Science Program, Faculty of Science & Engineering, Galala University, Suze 43511, Egypt  
<sup>6</sup> Department of Mathematics, Faculty of Science, Zagazig University, Zagazig 44519, Egypt  
\* Correspondence: marwa.elmahdi@hti.edu.eg

**Abstract:** In this paper, we present a newly modified machine learning model that employs a long short-term memory (LSTM) neural network model with the golden jackal optimization (GJO) algorithm to predict the tribological performance of Cu–Al<sub>2</sub>O<sub>3</sub> nanocomposites. The modified model was applied to predict the wear rates and coefficient of friction of Cu–Al<sub>2</sub>O<sub>3</sub> nanocomposites that were developed in this study. Electroless coating of Al<sub>2</sub>O<sub>3</sub> nanoparticles with Ag was performed to improve the wettability followed by ball milling and compaction to consolidate the composites. The microstructural, mechanical, and wear properties of the produced composites with different Al<sub>2</sub>O<sub>3</sub> content were characterized. The wear rates and coefficient of friction were evaluated using sliding wear tests at different loads and speeds. From a materials point of view, the manufactured composites with 10% Al<sub>2</sub>O<sub>3</sub> content showed huge enhancement in hardness and wear rates compared to pure copper, reaching 170% and 65%, respectively. The improvement of the properties was due to the excellent mechanical properties of Al<sub>2</sub>O<sub>3</sub>, grain refinement, and dislocation movement impedance. The developed model using the LSTM-GJO algorithm showed excellent predictability of the wear rate and coefficient of friction for all the considered composites.

**Keywords:** long short-term model; golden jackal optimization; Cu–Al<sub>2</sub>O<sub>3</sub> nanocomposites; tribological properties



**Citation:** Najjar, I.R.; Sadoun, A.M.; Fathy, A.; Abdallah, A.W.; Elaziz, M.A.; Elmahdy, M. Prediction of Tribological Properties of Alumina-Coated, Silver-Reinforced Copper Nanocomposites Using Long Short-Term Model Combined with Golden Jackal Optimization.

*Lubricants* **2022**, *10*, 277. <https://doi.org/10.3390/lubricants10110277>

Received: 28 September 2022

Accepted: 20 October 2022

Published: 24 October 2022

**Publisher's Note:** MDPI stays neutral with regard to jurisdictional claims in published maps and institutional affiliations.



**Copyright:** © 2022 by the authors. Licensee MDPI, Basel, Switzerland. This article is an open access article distributed under the terms and conditions of the Creative Commons Attribution (CC BY) license (<https://creativecommons.org/licenses/by/4.0/>).

## 1. Introduction

Properties that reduce friction are some of the most significant things to consider when constructing electronic circuits because they affect the quality of electronic components. The friction between two parts should be as low as feasible to reduce maintenance costs and extend the lifetime of the touched parts. In addition, the wear loss of the touched component surfaces should be kept to a bare minimum [1]. To that end, there has been a lot of focus on producing Cu-based nanocomposites with better frictional and wear resistances [2].

Copper and its alloys have been widely used in aviation, aerospace, and smart grid fields because of their excellent electrical and thermal conductivity as electrical connectors [3–7], which are mainly responsible for the power transfer and signals transmission of the system. However, the application of Cu is limited due to its low tribological properties such as poor wear resistance and inferior strength. Although copper matrix composites reinforced with ceramic fibers and/or particles exhibit a greater specific strength and elasticity

modulus, the electrical and thermal properties of the composites are usually reduced [8]. In this context, it is possible to manufacture mechanically strengthened Cu matrix composites by adding ceramic-based  $\text{Al}_2\text{O}_3$  [9–15], graphene [16–21], SiC [22,23],  $\text{ZrO}_2$  [24–28], and CNT [29,30] into the Cu matrix. Although the distribution of hard ceramic particles into the Cu matrix provides high hardness and durability to the composites, it causes a decrease in the electrical conductivity of the composites due to the presence of the ceramic particles to be distributed homogeneously in the metal matrix [31–33]. Moreover, the low conductivity of the ceramics plays a role in the conductivity reduction of the whole composite. Due to these disadvantages, it is stated that Cu should use second-phase elements (Al, Ni, Cr, Zn, Sn, etc.) or coatings in order to maintain good electrical properties while improving its physical and mechanical properties [34–38].

Because of their excellent hardness, wear, and corrosion resistance, ceramic materials reinforced by Cu-based nanocomposite coatings are currently being studied intensively. Cu-based nanocomposite coatings are deposited via high-velocity oxygen fuel spraying [39], plasma spraying [40], detonation thermal spraying [41], pulsed-gas dynamic spray [42], and cold spraying [43]. To produce Cu-based composite coatings, the precursor feedstock is reinforced with SiC,  $\text{B}_4\text{C}$ , and  $\text{Al}_2\text{O}_3$  [44]. An alumina nanoparticle is preferred because of its more stable structure and improved resistance to corrosion [45]. The amount, distribution, and size of reinforcing particles all have a significant effect on the composite's characteristics. Fathy et al. [46] found an increase in Cu– $\text{Al}_2\text{O}_3$  nanocomposites' compressive strength, wear resistance, and microhardness.

Wettability concerns make it difficult to form an interfacial bonding between metals and ceramics. Ceramics covered with metal powders are nanocomposite powders with a metallic shell and a ceramic core that convert non-metallic ceramic particles to metallic particles, adding specific magnetic, electrical, and chemical properties to the ceramic powders while also enhancing wettability between the metal and the ceramics [47,48]. To prevent Cu from oxidizing and improve Cu matrix mechanical properties, Cu matrix nanocomposites reinforced with  $\text{Al}_2\text{O}_3$ -coated Ag can be used [49,50].

Considering the applicability of Cu-based composites is related to many contact problems, such as those in brushes for wind turbine blades and electrodes, it is constructive to study their wear response under different conditions. The wear test is relatively expensive and time consuming because it runs several experiments at different loads and sliding speeds and distances. Thus, a rapid prediction tool based on experimental observations is valuable for industry. Because artificial intelligence has the advantage of providing solutions to very complex problems, regardless of lab availability or cost, it has been used to predict the wear rates of Cu– $\text{Al}_2\text{O}_3$  nanocomposites under abrasive wear conditions [51–54]. A recent work utilized an enhanced dendritic neural algorithm to predict the wear behavior of Cu– $\text{Al}_2\text{O}_3$  nanocomposites [55]. Furthermore, machine learning finds applications in engineering, chemistry, and other fields [56–59]. The newly developed random vector functional link (RVFL) algorithm was trained using experimental data from wear tests to accurately predict the response of this composite with different  $\text{Al}_2\text{O}_3$  content.

Moreover, the performance of long short-term memory (LSTM) has been established as a ML technique and applied to different applications, for example, viral reverse engineering [60], wind power [61], and others [62,63]. However, the main limitation of LSTM is the difficulty in determining the parameters that have the largest influence on its performance. So, this motivated us to propose an alternative method to handle this limitation by using a metaheuristic technique named golden jackal optimization (GJO) [64]. The main aim of using GJO was to find the optimal value for the parameters of the LSTM to enhance its performance.

The main objective of the paper was to predict the wear behavior of Cu– $\text{Al}_2\text{O}_3$  nanocomposites using a newly adapted machine learning model named long short-term memory (LSTM) based on GJO. Based on the foregoing analysis, Cu– $\text{Al}_2\text{O}_3$ -covered Ag with varying  $\text{Al}_2\text{O}_3$  contents was fabricated in the current study using silver nanoparticles electrolessly deposited on alumina. The nanocomposite coatings' microstructural and mi-

microhardness were investigated. After that, the effects of adding  $\text{Al}_2\text{O}_3$ -coated nanoparticles to the nanocomposite coatings on tribological behavior were examined. Finally, the LSTM algorithm was trained to predict the wear and frictional properties of various composites with a wider range of reinforcement content. The application of this technique will aid in the development of these composites for military and medical applications [65,66].

## 2. Experimental Procedure

The nanocomposite was created using copper powder (particle size of ~50 nm and 99.99% purity) as a metal matrix and  $\text{Al}_2\text{O}_3$  ( $\gamma\text{-Al}_2\text{O}_3$ , 99.99%, 50 nm) as a ceramic reinforcing ingredient. To verify the interface qualities,  $\text{Al}_2\text{O}_3$  was coated onto Ag using an electroless plating technique. Sensitization of alumina was performed by drowning it in a 5 percent sodium hydroxide solution and moving it for 1.5 h, then immersing it into acetone for 1.5 h using an ultrasonic cleaner. This gel was then dried for 1 h at 125 °C in an oven. Then, electroless deposition of Ag on alumina was performed using a chemical bath containing a 3 g/L silver nitrate solution and 300 mL/L formaldehyde with a pH of 12. For 15 min, a magnetic stirrer was used to mix the solution continuously at 25 degrees Celsius. This gel was rinsed and dried for 1.5 h at 125 °C. The gel was then solidified. Nanoparticles were reinforced with copper powder of various weights (0, 2.5, 5, 7.5, and 10) to create nanocomposites via the powder metallurgy route (ball milling and consolidation). Under 700 MPa, the mixture was cold compacted with the use of a hydraulic press and punch and die. To reduce die-to-punch friction, the punch and die were carefully cleaned with acetone and lubricated with zinc stearate before compacting each sample. After that, the samples were sintered in hydrogen for 90 min at 950 degrees Celsius.

The morphological and microstructural properties of compact samples were examined using a Zeiss Evo LS10-type scanning electron microscope (SEM). Aztec One system EDS System was used for elemental mapping tests. All sintered nanocomposite contacts were hardness tested using the Shimadzu digital Vickers microhardness method at a 5 N load for 10 s. To ensure the repeatability of the test results, four measurements were taken for each sample.

Pin-on-disk wear equipment was used to evaluate the specimens' wear resistance. The samples were cleaned with ethanol before testing to remove any impurities. The pin and disk were made of AISI 52,100 steel (with a hardness of 63 HRC) and the sample, respectively. The tests of wear were conducted at various speeds (0.4, 0.8, and 1.2 m/s) and under various standard loads of 10, 20, 30, and 40 N. The loss of weight was measured every 2 min using an analytical balance with a 0.1 mg precision. Before and after each interval of the wear testing, the pins were cleaned with alcohol. The micro-computer-controlled vertical universal friction and wear tester was used to test the wear coefficient of  $\text{Cu-Al}_2\text{O}_3$  nanocomposite coatings. The friction coefficient was calculated using the friction torque measured while sliding.

## 3. Machine Learning Model

### 3.1. Long Short-Term Memory Neural Network Model

A description of long short-term memory (LSTM) is given in this section. The LSTM is viewed as an enhanced version of the current neural network (RNN) that goes beyond the drawbacks of the conventional RNN [67]. LSTM excels in remembering vast volumes of information over extended periods and learning dependencies. A typical LSTM model has a large number of modules in its chain structure. These modules differ from conventional RNNs in that they include four distinct interaction levels that are all uniquely coupled. Figure 1 shows the LSTM's configuration and includes a cell that represents the memory modules. The condition of the cell determines how data flow forward. It is possible to apply some linear transformations to the data. The activation gates can also be used to add or remove information from the cell state. These activation gates are used to apply sigmoid activation functions to the data. Each gate uses a unique set of weights and a variety of

matrices operations. These gates are additionally utilized to control the memory process, enhancing the LSTM's capabilities and preventing dependence problems.

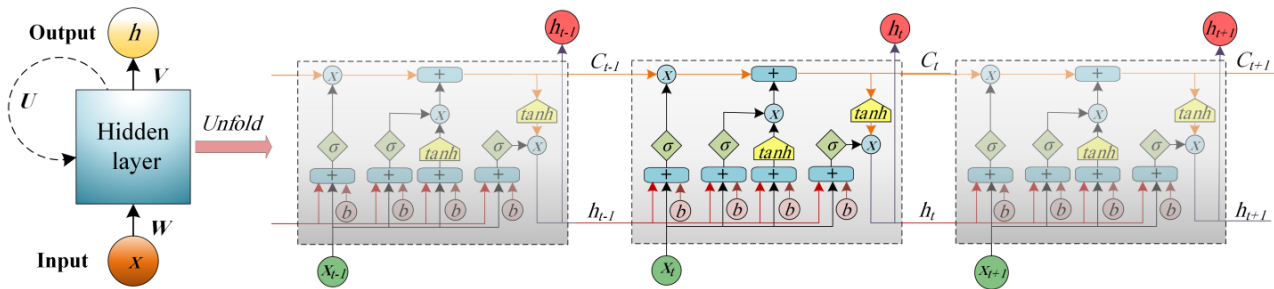


**Figure 1.** The structure of a typical LSTM neural network.

The input from the current state and the hidden state of the previous cell is first passed to the forget gate to decide whether to store the information by outputting one or discard it by outputting zero, as illustrated in Figure 1.  $X$  is the input vector at time  $t$ , and  $N$  is the number of LSTM cells in the forward pass in Equation (1). Choosing whether or not to forget the knowledge is the primary goal of forget gates. The sum of the bias ( $b_f$ ) and the product between the weights ( $W_f$ ) and the inputs ( $h_{t-1}, X_t$ ), which includes the input from the previous state ( $h_{t-1}$ ) and then the forget value ( $f_t$ ), is defined as:

$$f_t = \sigma(W_f \cdot [h_{t-1} X_t] + b_f) \quad (1)$$

The following step involves utilizing the following equation to update the cell state ( $C_t$ ):

$$C_t = C_{t-1} \cdot f_t + N_t \cdot i_t \quad (2)$$

where  $N_t$  denotes the output of the tanh function that depends on  $W_n, h_{t-1}, X_t$ , and  $b_n$ , and it is computed as:

$$N_t = \tan h(W_n \cdot [h_{t-1}, X_t] + b_n) \quad (3)$$

where  $i_t$  is the output of sigmoid layer, which is calculated using the following formula:

$$i_t = \sigma(W_i \cdot [h_{t-1}, X_t] + b_n) \quad (4)$$

After that, the sigmoid activation output ( $O_t$ ) is calculated based on the value of  $X_t, h_{t-1}, W_o$ , and  $b_o$ , as formulated in Equation (5):

$$O_t = \sigma(W_o \cdot [h_{t-1}, X_t] + b_o) \quad (5)$$

The next step is to enhance the value of  $h_t$ , as defined in Equation (6):

$$h_t = O_t \cdot \tan h(C_t) \quad (6)$$

### 3.2. Golden Jackal Optimization (GJO)

In this part, the steps of the golden jackal optimization (GJO) algorithm [64] are presented. Similar to other metaheuristic (MH) techniques, the first process in GJO is to construct the population of  $N$  solutions using the following formula:

$$X_i = LB + r \times (UB - LB), i = 1, 2, \dots, N \quad (7)$$

where  $LB$  and  $UB$  are the limits of parameters within the search space.  $r \in [0, 1]$  denotes the random value. After that, for each  $X_i, i = 1, 2, \dots, N$ , the fitness value, and determines

the best of them (i.e., male solution  $X_b$ ) and second best (i.e., female jackal). The next step is to build the matrix of prey using Equation (8):

$$Prey = \begin{bmatrix} X_{11} & X_{12} & \dots & X_{1d} \\ X_{21} & X_{22} & \dots & X_{2d} \\ \vdots & \vdots & \vdots & \vdots \\ X_{N1} & X_{N2} & \dots & X_{Nd} \end{bmatrix} \quad (8)$$

### 3.2.1. Exploration Stage

The hunting process is the simulation of exploration, and this depends on the male jackal ( $X_M$ ) and female jackal ( $X_{FM}$ ) updating their position according to  $X_M$ . This process can be formulated using Equations (9) and (10):

$$X_1(t) = X_M(t) - E \times |X_M(t) - r_l \times Prey(t)| \quad (9)$$

$$X_2(t) = X_{FM}(t) - E \times |X_{FM}(t) - r_l \times Prey(t)| \quad (10)$$

where  $X_M$  and  $X_{FM}$  are updated to  $X_1$  and  $X_2$ , respectively, at the  $t$ -th iteration.  $E$  is the energy of prey which is updated as:

$$E = E_0 \times E_1 \quad (11)$$

In Equation (11),  $E_1$  and  $E_0$  are the decreasing and initial value of energy, respectively. The values of  $E_0$  and  $E_1$  are updated using Equations (12) and (13), respectively:

$$E_0 = 2 \times r - 1 \quad (12)$$

$$E_1 = c_1 \times (1 - (t/T)) \quad (13)$$

In Equation (13),  $T$  refers to the maximum number of generations. Meanwhile,  $r_l$  refers to random value produced according to the Levy distribution using Equation (14):

$$r_l = 0.05 \times Levy \quad (14)$$

After that, the positions of the jackal are updated according to Equation (15):

$$X(t+1) = \frac{X_1(t) + X_2(t)}{2} \times Levy, Levy = \frac{s|u \times \sigma|}{|v|^{\frac{1}{\beta}}}, \sigma = \left( \frac{\Gamma(1+\beta) \times \sin\left(\frac{\pi\beta}{2}\right)}{\Gamma\left(\frac{1+\beta}{2}\right) \times \beta \times 2^{\left(\frac{\beta-1}{2}\right)}} \right) \quad (15)$$

where  $u$  and  $v$  refer to random numbers; in addition,  $\beta = 1.5$  and  $s = 0.01$  are constants.

### 3.2.2. Exploitation Stage

Within the exploitation phase, GJO aims to discover feasible solutions within the explored areas. This process in GJO represents the hunting of male and female jackals in nature, and the mathematical definition is given as:

$$X_1(t) = X_M(t) - E \times |r_l \times X_M(t) - Prey(t)| \quad (16)$$

$$X_2(t) = X_{FM}(t) - E \times |r_l \times X_{FM}(t) - Prey(t)| \quad (17)$$

### 3.2.3. Switching from Exploration to Exploitation

In GJO, the transition between the exploration and exploitation phases is accomplished by utilizing the prey's escaping energy. If the value of  $|E| > 1$ , the solutions commence their exploration phase; if not, they move on to the exploitation phase. The GJO steps are shown in Figure 2.

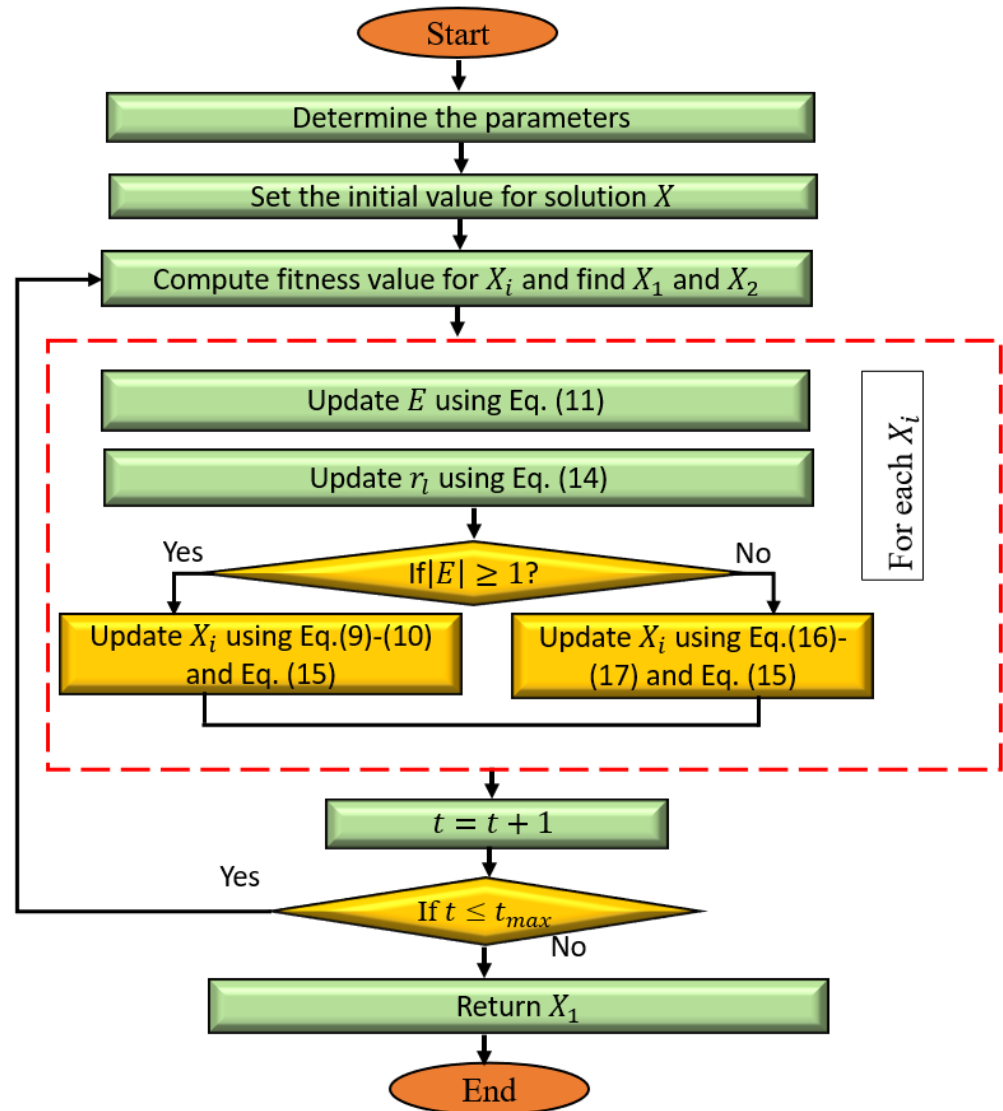


Figure 2. The GJO algorithm steps.

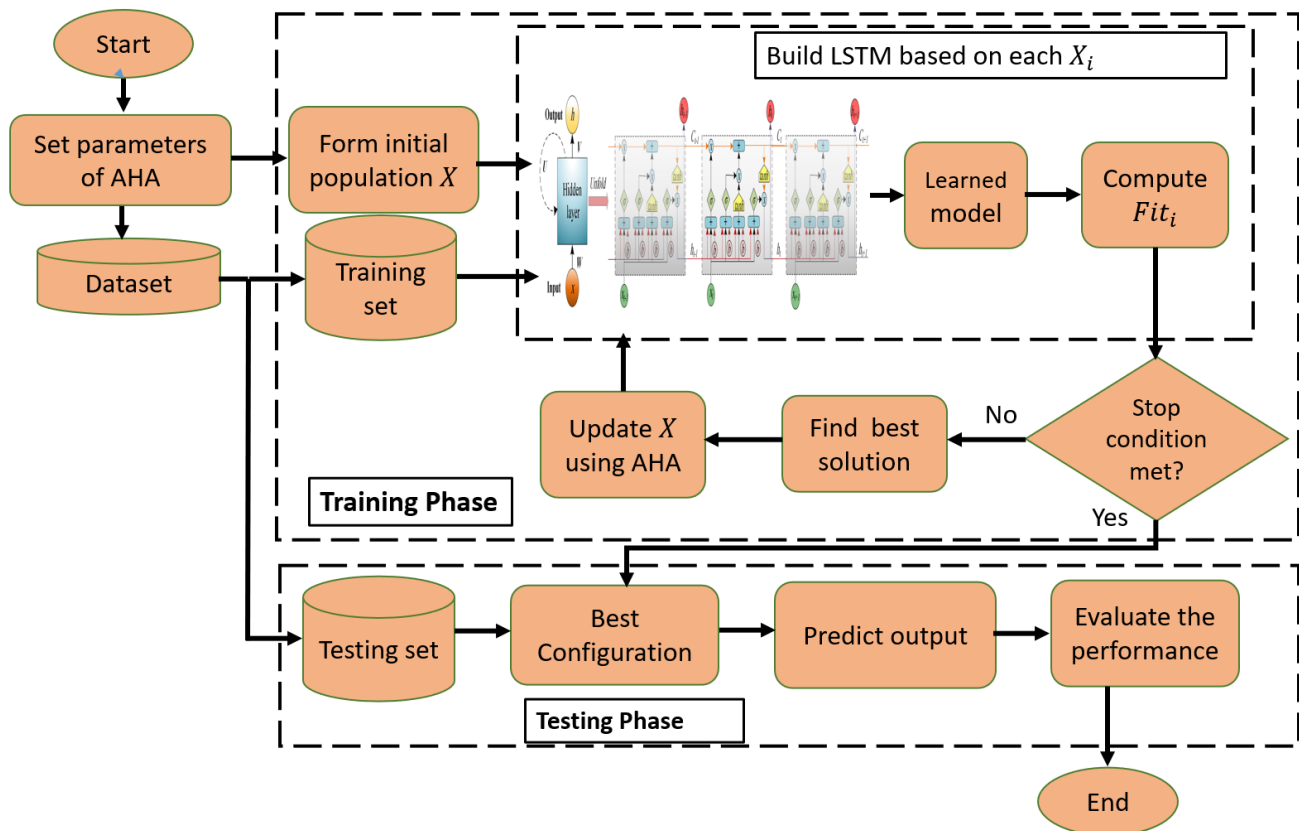
### 3.3. Proposed Model

Figure 3 shows the steps of the tribological properties prediction model. In summary, the provided model, known as LSTM-GJO, relies on exploiting the GJO algorithm's behavior to establish the LSTM network's parameters.

The first step in LSTM-GJO is to use the following equation to produce the initial solutions, which represent the value of each LSTM parameter:

$$X_{ij} = l_j + r \times (u_j - l_j), \quad i = 1, \dots, N, \quad j = 1, \dots, D, \quad r \in [0, 1] \quad (18)$$

where  $u_j$  and  $l_j$  are limits of the parameter of the LSTM. In this study,  $D = 5$  is the number of parameters in  $X_i$ , which refers to minimum batch size ( $B_S$ ), number of hidden units ( $N_h$ ), learn rate drop factor ( $LRD_F$ ), max epochs ( $Max_E$ ), and optimization approach ( $Op_M$ ). In this study, we set  $Op_M \in \{1, 2, 3\}$ , which refers to Adam, the stochastic gradient descent with momentum (SGDM), and the RMSProp optimizer, respectively, as well as  $LRD_F \in [0.1, 0.9]$ ,  $N_h \in [20, 200]$ ,  $B_S \in [64, 265]$ , and  $Max_E \in [20, 300]$ . For clarity, suppose  $X_i = [B_S, N_h, LRD_F, Max_E, Op_M] = [64, 25, 0.5, 200, 1]$ , which refers to Adam optimizers, is used with  $N_h = 200$ ,  $B_S = 64$ ,  $LRD_F = 0.5$ , and  $Max_E = 200$  as the structure of the LSTM.



**Figure 3.** Structure of LSTM- GJO model used to predict the tribological properties of the composites.

Thereafter, the fitness value of  $X_i$  is computed according to the training set that represents 70% of the samples of input data.

$$Fit_i = \sqrt{\frac{\sum_{i=1}^{N_s} (Y_P - Y_T)^2}{N_s}} \quad (19)$$

where  $N_s$  is the number of instances in the training set with the output  $Y_T$ , whereas  $Y_P$  is the predicted output. After choosing the best solution, we update the other solutions using the operators of the GJO. This update stage is continued until we reach the stop conditions and returns the best solution. Employing performance metrics to assess the best solution is performing using the testing set, which represents 30% of the input data.

## 4. Results and Discussion

### 4.1. Microstructural Observations

Figure 4 shows the morphology and the composition of Cu–Al<sub>2</sub>O<sub>3</sub> nanocomposite powders with different Al<sub>2</sub>O<sub>3</sub> content after ball milling. The Cu particles became smaller with increasing Al<sub>2</sub>O<sub>3</sub> content. Moreover, the particle shape became rounded and uniformly distributed with increasing Al<sub>2</sub>O<sub>3</sub> content, as shown in Figure 4c. The presence of Al<sub>2</sub>O<sub>3</sub> nanoparticles in the mixture during milling accelerates the fracture process of the Cu particles due to the reduction of plasticity of the material caused by severe impacts and the penetration of Al<sub>2</sub>O<sub>3</sub> nanoparticles to the lattice structure of Cu particles [68,69]. During the milling process, Al<sub>2</sub>O<sub>3</sub> nanoparticles stick to Cu particles, which reduces their plasticity and facilitates their fracture [68]. The reduction of Cu particle size and the uniform distribution of the Al<sub>2</sub>O<sub>3</sub> nanoparticles at the particle scale play a great role in the production of homogenous composites with good dispersion of Al<sub>2</sub>O<sub>3</sub> nanoparticles. The XRD analysis of all Cu–Al<sub>2</sub>O<sub>3</sub>-nanocomposites-coated Ag showed the presence of Cu, Al<sub>2</sub>O<sub>3</sub>, and Ag,

which were the main components of the produced composite, without any observable contaminants, Figure 4d.

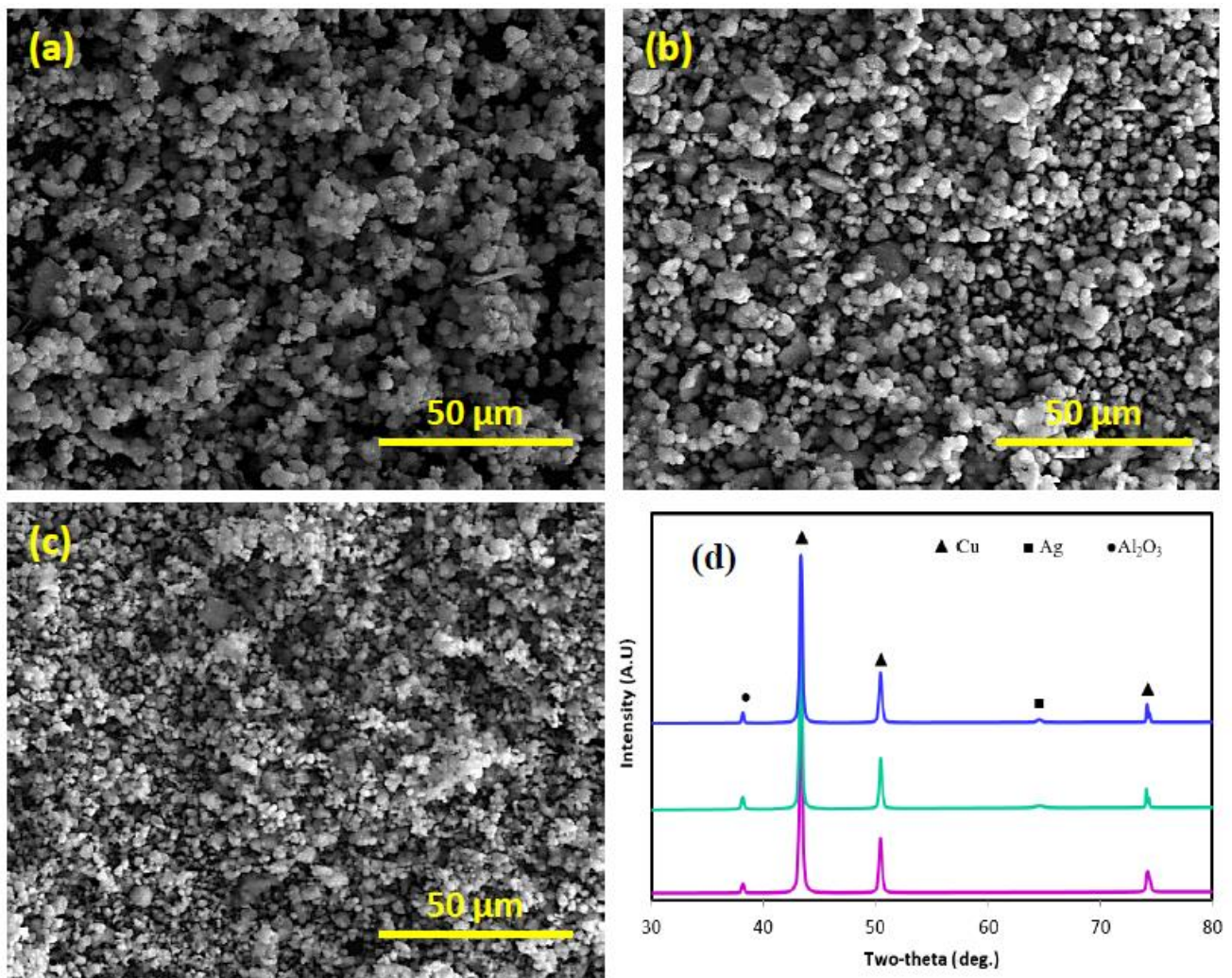


**Figure 4.** SEM micrograph of the nanocomposite powders; (a) Cu–2.5%Al<sub>2</sub>O<sub>3</sub>-coated Ag, (b) Cu–5%Al<sub>2</sub>O<sub>3</sub>-coated Ag, (c) Cu–10%Al<sub>2</sub>O<sub>3</sub>-coated Ag, (d) XRD of all Cu–10%Al<sub>2</sub>O<sub>3</sub>-coated Ag.

Figure 5 shows the microstructure of the produced bulk Cu–Al<sub>2</sub>O<sub>3</sub> nanocomposites after consolidation. The microstructure of the consolidated samples revealed a dense composite with low void content due to the homogeneity of the microstructure. Moreover, there was no agglomeration of Al<sub>2</sub>O<sub>3</sub> nanoparticles observed. The absence of micro-sized agglomeration was due to the coating of the Al<sub>2</sub>O<sub>3</sub> nanoparticles with Ag, which improved their wettability with Cu, as previously reported in [29,30,70]. The good dispersion of Al<sub>2</sub>O<sub>3</sub> nanoparticles in the consolidated samples was a subsequent result of the good dispersion and the absence of agglomeration in the powder form of the composite (see Figure 4). Coating Al<sub>2</sub>O<sub>3</sub> nanoparticles with Ag particles reduced the mismatch of the surface characteristics between Cu and Al<sub>2</sub>O<sub>3</sub>, which enhanced the adhesion between Cu grains and Al<sub>2</sub>O<sub>3</sub> nanoparticles, as shown in Figure 5d. Thus, a void-free microstructure was produced. The grain size was observed to be reduced with increasing Al<sub>2</sub>O<sub>3</sub> content. The reduction of grain size was attributed to the increase of Al<sub>2</sub>O<sub>3</sub> content that precipitated at the Cu grain boundaries, which reduced the relative movement and relaxation of grains during solidification. Previous studies explained the mechanism of consolidation of Cu-based composite reinforced with Al<sub>2</sub>O<sub>3</sub> coated by Ag and Ni nanoparticles,

and they demonstrated the efficiency of this process to improve the wettability of these composites [70,71].

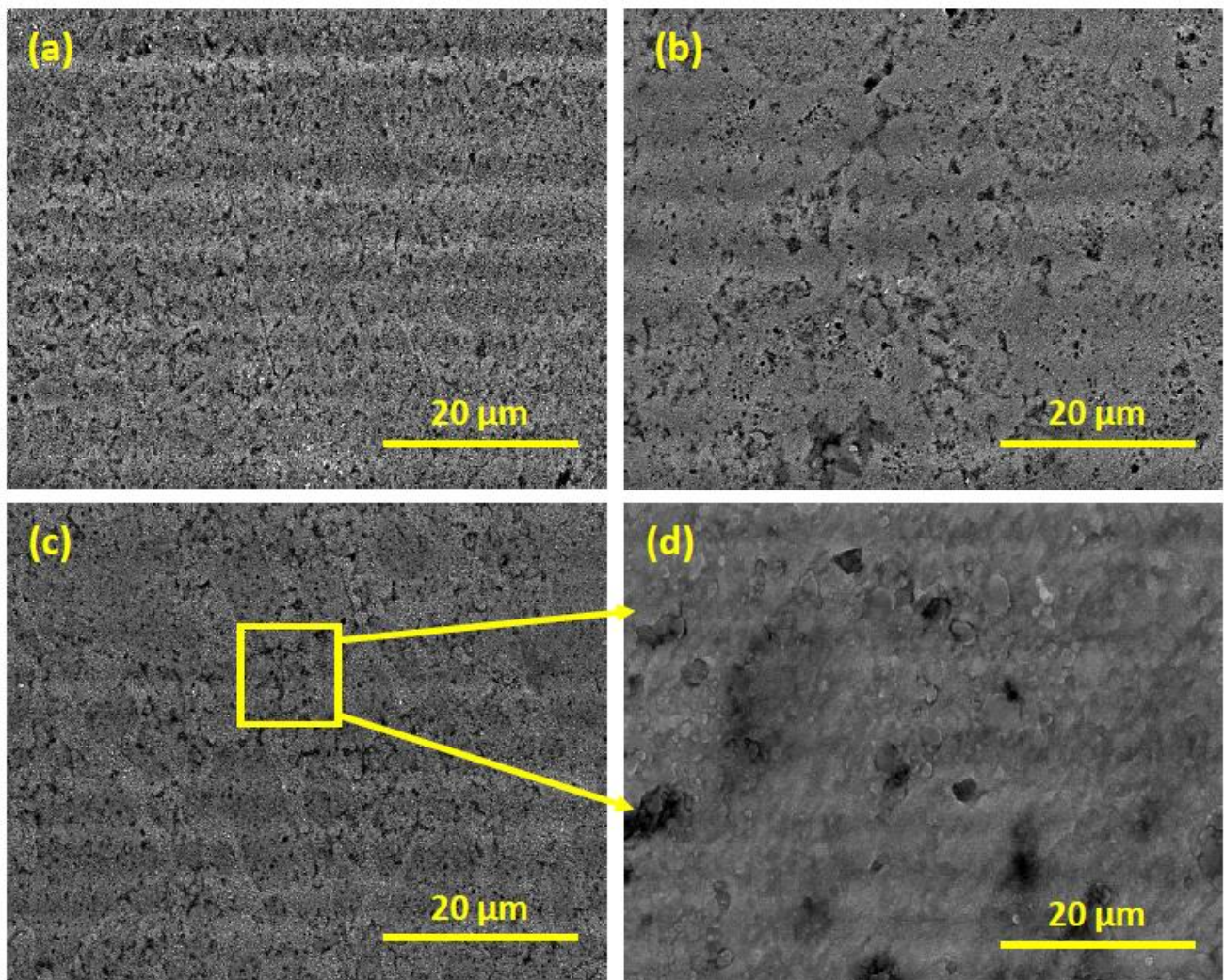


**Figure 5.** SEM micrographs of nanocomposites of (a) Cu-2.5%Al<sub>2</sub>O<sub>3</sub>-coated Ag, (b) Cu-5%Al<sub>2</sub>O<sub>3</sub>-coated Ag, (c) Cu-10%Al<sub>2</sub>O<sub>3</sub>-coated Ag, (d) larger magnification of Cu-10%Al<sub>2</sub>O<sub>3</sub>-coated Ag.

In order to ensure homogenous distribution at the element level, EDS and mapping analysis were conducted, and the results are reported in Figure 6. After consolidation, the mapping analysis showed the homogenous distribution of the reinforcement in the matrix at the element level, where no agglomeration of any of the composite elements was observed. Moreover, it demonstrated that the produced composite was free from any contaminants that might have occurred during consolidation and sintering.

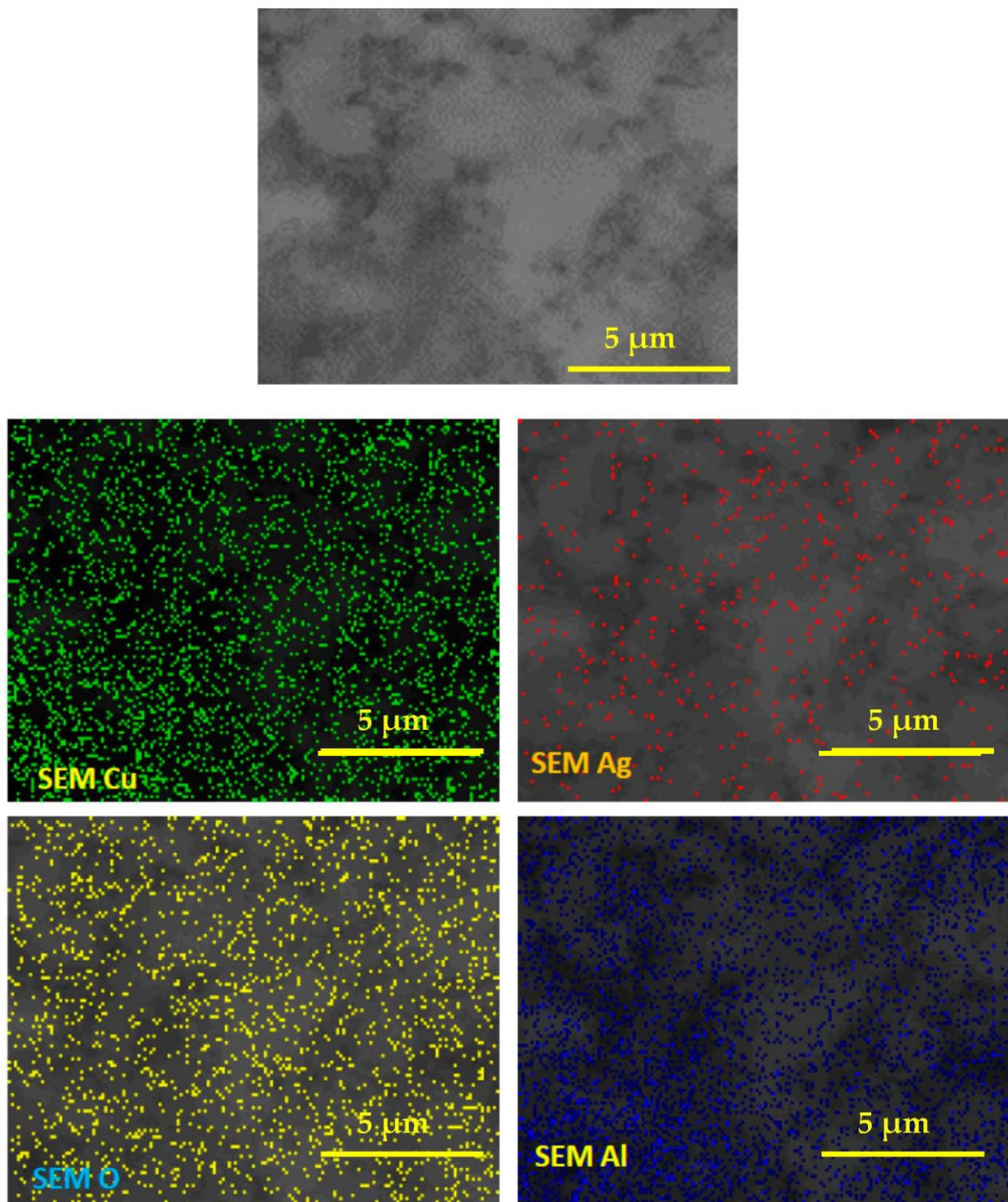


Figure 6. SEM mapping of the Cu-10%Al<sub>2</sub>O<sub>3</sub>-coated Ag nanocomposite.

#### 4.2. Microhardness

As illustrated in Figure 7, the relative density decreased with increasing Al<sub>2</sub>O<sub>3</sub> mass fraction, decreasing from 97.5 to 93.8 for the Cu matrix and the specimen with 10% Al<sub>2</sub>O<sub>3</sub>. The microhardness of Cu–Al<sub>2</sub>O<sub>3</sub> nanocomposites with different Al<sub>2</sub>O<sub>3</sub> nanoparticles content was evaluated, as shown in Figure 7. The microhardness of the pure Cu samples was 63.9 HV. The addition of 2.5% Al<sub>2</sub>O<sub>3</sub> nanoparticles led to an increase in the hardness to 72.4 HV. This hardness increase was attributed to the addition of Ag-coated Al<sub>2</sub>O<sub>3</sub> nanoparticles, which impeded the dislocation movement during indentation. Moreover, the

existence of  $\text{Al}_2\text{O}_3$  nanoparticles in the composite microstructure reduced the plastic deformation ability of the material during indentation, which reduced the indentation depth and, hence, increased the material hardness. The microhardness increased with increasing  $\text{Al}_2\text{O}_3$  nanoparticles content, reaching 165 HV for the composite with 10%  $\text{Al}_2\text{O}_3$  content. The good dispersion of  $\text{Al}_2\text{O}_3$  nanoparticles with extremely high hardness inside the Cu matrix (see Figure 5) was the main reason for the hardness improvement. Moreover, the reduction of the grain size contributed to the reduction in the material plasticity, which enhanced the hardness as well [72]. Additionally, increasing the  $\text{Al}_2\text{O}_3$  content increased the impedance of dislocation movement, which contributed to the hardness improvement [72]. Compared to other available composites in the literature, where Cu- $\text{Al}_2\text{O}_3$  was reinforced with 2% GNPs particles, the improvement rate for Cu- $\text{Al}_2\text{O}_3$  coated with silver particles showed a 1.5 times larger improvement rate compared to Cu- $\text{Al}_2\text{O}_3$  [20].

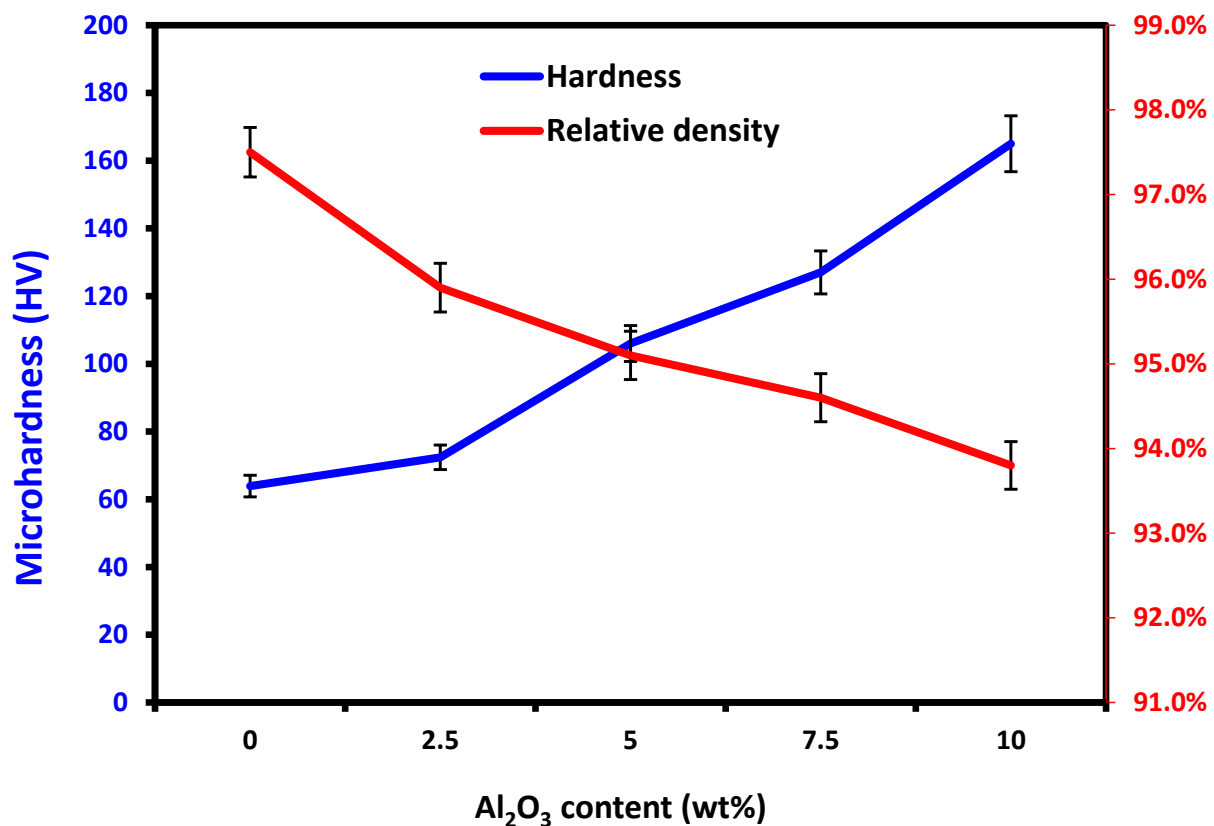


Figure 7. Variation of microhardness and relative density of nanocomposites versus alumina content.

#### 4.3. Tribological Properties

Table 1 shows the wear rates of the Cu- $\text{Al}_2\text{O}_3$  nanocomposites with different  $\text{Al}_2\text{O}_3$  content tested at different loads and sliding speeds. The addition of  $\text{Al}_2\text{O}_3$  nanoparticles to the Cu matrix reduced the wear rates for all the considered loads and speeds. For instance, the wear rate of the composite with 3%  $\text{Al}_2\text{O}_3$  content tested under 20 N load and 0.3 m/s sliding speed was  $3.4 \times 10^{-5}$  g/m compared to  $4.2 \times 10^{-5}$  g/m for pure Cu, which achieved 24% wear rate reduction. The existence of  $\text{Al}_2\text{O}_3$  nanoparticles in the composite microstructure enhanced the hardness of the material (see Figure 7), which increased the ability of the material to resist sliding pins. Moreover, the reduction of the material plasticity caused by the addition of  $\text{Al}_2\text{O}_3$  and grain refinement reduced the material removal rate during sliding, which enhanced the wear rates. Increasing the  $\text{Al}_2\text{O}_3$  content reduced the wear rate of the composite, reaching around 70% improvement for the composite with 12%  $\text{Al}_2\text{O}_3$  content. This response was predicted because of the improvement of the hardness and the homogenous microstructure of this composite.

**Table 1.** Tribological properties of Cu–Al<sub>2</sub>O<sub>3</sub> nanocomposites. The data in parenthesis represent the standard deviation of the results.

Load (N)	Wear Rates $\times 10^{-5}$ g/m														
	Sliding Speed 0.4 m/s					0.8 m/s					1.2 m/s				
	0%	2.5%	5%	7.5%	10%	0%	2.5%	5%	7.5%	10%	0%	2.5%	5%	7.5%	10%
10	3.7 $\pm$ 0.2	3.0 $\pm$ 0.1	2.6 $\pm$ 0.2	1.7 $\pm$ 0.1	1.1 $\pm$ 0.2	4.3 $\pm$ 0.1	4.1 $\pm$ 0.2	3.5 $\pm$ 0.1	3.0 $\pm$ 0.1	2.7 $\pm$ 0.1	4.6 $\pm$ 0.2	4.4 $\pm$ 0.2	3.8 $\pm$ 0.1	3.2 $\pm$ 0.2	3.1 $\pm$ 0.1
20	4.2 $\pm$ 0.1	3.4 $\pm$ 0.2	2.8 $\pm$ 0.1	1.9 $\pm$ 0.2	1.4 $\pm$ 0.1	5.8 $\pm$ 0.2	4.8 $\pm$ 0.1	4.2 $\pm$ 0.2	3.6 $\pm$ 0.2	3.1 $\pm$ 0.1	5.9 $\pm$ 0.2	5.0 $\pm$ 0.1	4.5 $\pm$ 0.2	3.9 $\pm$ 0.1	3.3 $\pm$ 0.1
30	4.4 $\pm$ 0.1	3.8 $\pm$ 0.1	3.0 $\pm$ 0.2	2.4 $\pm$ 0.1	1.6 $\pm$ 0.2	6.5 $\pm$ 0.1	5.5 $\pm$ 0.2	5.0 $\pm$ 0.1	4.2 $\pm$ 0.2	3.6 $\pm$ 0.1	7.2 $\pm$ 0.2	5.8 $\pm$ 0.2	5.4 $\pm$ 0.1	4.6 $\pm$ 0.1	3.5 $\pm$ 0.1
40	5.1 $\pm$ 0.3	4.2 $\pm$ 0.2	3.2 $\pm$ 0.1	2.2 $\pm$ 0.2	1.8 $\pm$ 0.1	8.0 $\pm$ 0.2	6.9 $\pm$ 0.1	6.2 $\pm$ 0.2	5.4 $\pm$ 0.1	4.1 $\pm$ 0.1	8.58 $\pm$ 0.3	7.5 $\pm$ 0.3	6.3 $\pm$ 0.2	5.3 $\pm$ 0.1	3.8 $\pm$ 0.1
Coefficient of Friction															
10	0.81 $\pm$ 0.02	0.78 $\pm$ 0.01	0.77 $\pm$ 0.02	0.74 $\pm$ 0.02	0.70 $\pm$ 0.01	0.72 $\pm$ 0.01	0.70 $\pm$ 0.02	0.68 $\pm$ 0.02	0.65 $\pm$ 0.02	0.63 $\pm$ 0.01	0.60 $\pm$ 0.01	0.58 $\pm$ 0.01	0.56 $\pm$ 0.01	0.54 $\pm$ 0.02	0.53 $\pm$ 0.02
20	0.78 $\pm$ 0.02	0.75 $\pm$ 0.03	0.73 $\pm$ 0.02	0.71 $\pm$ 0.03	0.68 $\pm$ 0.02	0.71 $\pm$ 0.01	0.69 $\pm$ 0.02	0.66 $\pm$ 0.02	0.62 $\pm$ 0.01	0.61 $\pm$ 0.01	0.58 $\pm$ 0.01	0.56 $\pm$ 0.02	0.53 $\pm$ 0.01	0.51 $\pm$ 0.02	0.50 $\pm$ 0.01
30	0.76 $\pm$ 0.02	0.73 $\pm$ 0.02	0.71 $\pm$ 0.02	0.66 $\pm$ 0.03	0.65 $\pm$ 0.01	0.68 $\pm$ 0.02	0.67 $\pm$ 0.01	0.64 $\pm$ 0.02	0.60 $\pm$ 0.01	0.58 $\pm$ 0.02	0.57 $\pm$ 0.01	0.53 $\pm$ 0.02	0.51 $\pm$ 0.01	0.48 $\pm$ 0.02	0.47 $\pm$ 0.01
40	0.74 $\pm$ 0.02	0.71 $\pm$ 0.03	0.68 $\pm$ 0.02	0.63 $\pm$ 0.03	0.60 $\pm$ 0.01	0.66 $\pm$ 0.02	0.64 $\pm$ 0.01	0.62 $\pm$ 0.02	0.58 $\pm$ 0.01	0.56 $\pm$ 0.02	0.55 $\pm$ 0.01	0.51 $\pm$ 0.01	0.50 $\pm$ 0.01	0.47 $\pm$ 0.01	0.44 $\pm$ 0.01

The testing conditions affected the wear rates, as shown in Figure 5, and increasing the testing load led to an increase in the wear rates. This was due to the increase of material removal during sliding that was caused by the larger pressure applied to the pin, which allowed larger plastic deformations [73]. The same behavior was observed for the sliding speed, where increasing the sliding speed led to an increase in the wear rates due to the larger friction forces generated between the disk and the pin, which allowed larger material removal rates.

The effect of  $\text{Al}_2\text{O}_3$  content, testing load, and sliding speed on the coefficient of friction of Cu– $\text{Al}_2\text{O}_3$  nanocomposites is shown in Table 1. The additions of  $\text{Al}_2\text{O}_3$  nanoparticles highly influenced the coefficient of friction of the produced composite, and a clear reduction of the friction coefficient was observed with increasing  $\text{Al}_2\text{O}_3$  content. This was due to the lower plastic deformation of the composites compared to the pure Cu caused by the grain refinement and presence of  $\text{Al}_2\text{O}_3$  nanoparticles, which reduced the contact area between the disk and the pin. The effect of testing load and sliding speed was opposite to their effect on the wear rates, as shown in the figure. For such cases where many parameters control the test with a global trend, an analytical model that combines the effect of the reinforcement weight fraction and the testing condition could help for reducing experimental cost and time. However, there are no analytical models that consider all these parameters. Therefore, a machine learning model could be applied to predict the response based on the training set that we tested.

Table 2 and Figures 8 and 9 show the comparison between the presented LSTM-GJO and other methods, such as asymptotic organisms search (SOS) [74], the grey wolf algorithm (GWO) [75], and the salp swarm algorithm (SSA) [76], for wear rates prediction considering the effect of  $\text{Al}_2\text{O}_3$  content and testing conditions. The comparison between the GJO and other models was computed using three well-known performance measures named the root-mean-square error (RMSE), the mean absolute error (MAE), and the coefficient of determination  $R^2$ . The results showed that the performance of the LSTM-GJO was superior to the other methods in the two tested outputs, wear rate and coefficient of friction. For example, in the case of wear rate, the LSTM-GJO provided an  $R^2$  higher than SOS, GWO, and SSA, being 6.88, 3.49, and 3.02, respectively, whereas the  $R^2$  of the LSTM-GJO was nearly 5.25, 3.59, and 3.78 higher than SOS, GWO, and SSA, respectively. In addition, by comparing the value of RMSE and MAE in the two cases, we noticed that LSTM-GJO had a smaller value than other methods. This indicates that LSTM-GJO has a greater ability to predict wear rates and coefficient of friction than other methods. Moreover, this observation can be seen in Figures 8 and 9, which show the correlation between the predicted wear rates and coefficient of friction obtained using LSTM-GJO and other methods.

**Table 2.** Predictability of LSTM-GJO model compared to other models.

	Wear Rates				Coefficient of Friction			
	GJO	SOS	GWO	SSA	GJO	SOS	GWO	SSA
$R^2$	0.9896	0.9493	0.8827	0.8999	0.9950	0.9915	0.9828	0.9911
RMSE	0.0531	0.1171	0.1782	0.1646	0.3677	0.4814	0.6845	0.4929
MAE	0.0509	0.1110	0.1774	0.1603	0.2604	0.3311	0.5248	0.3904

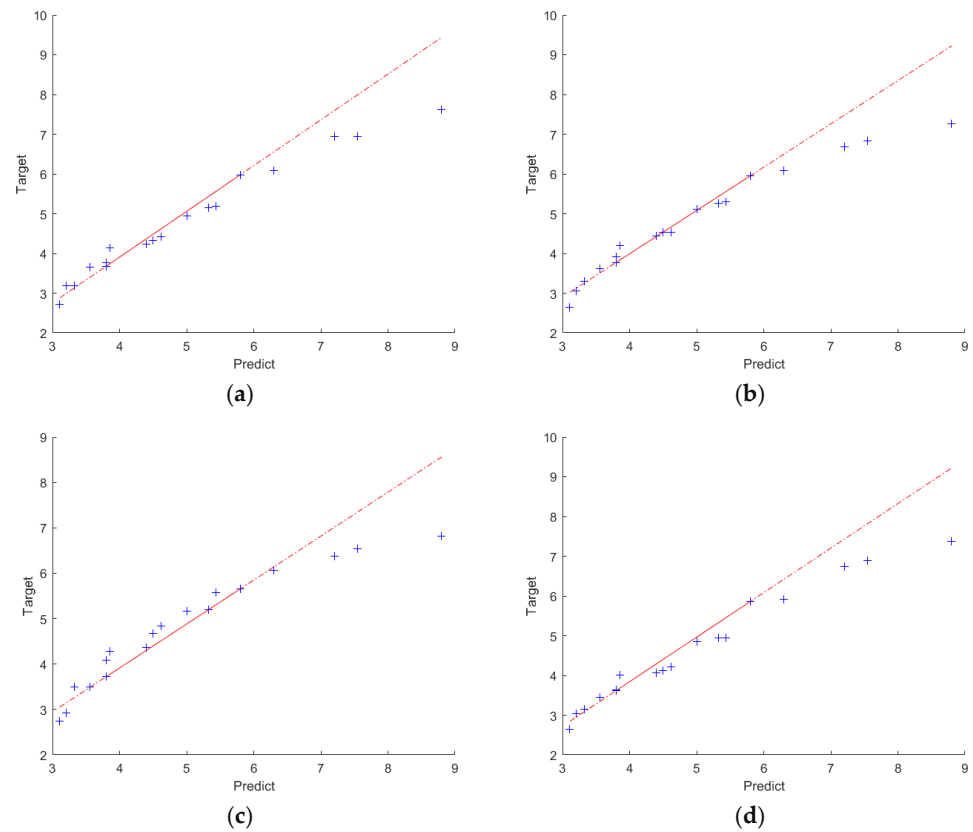


**Figure 8.** Quantile–quantile (QQ) plot between the wear rate and its predicted value obtained by the algorithms. (a). GJO. (b). SOS. (c). GWO. (d). SSA.

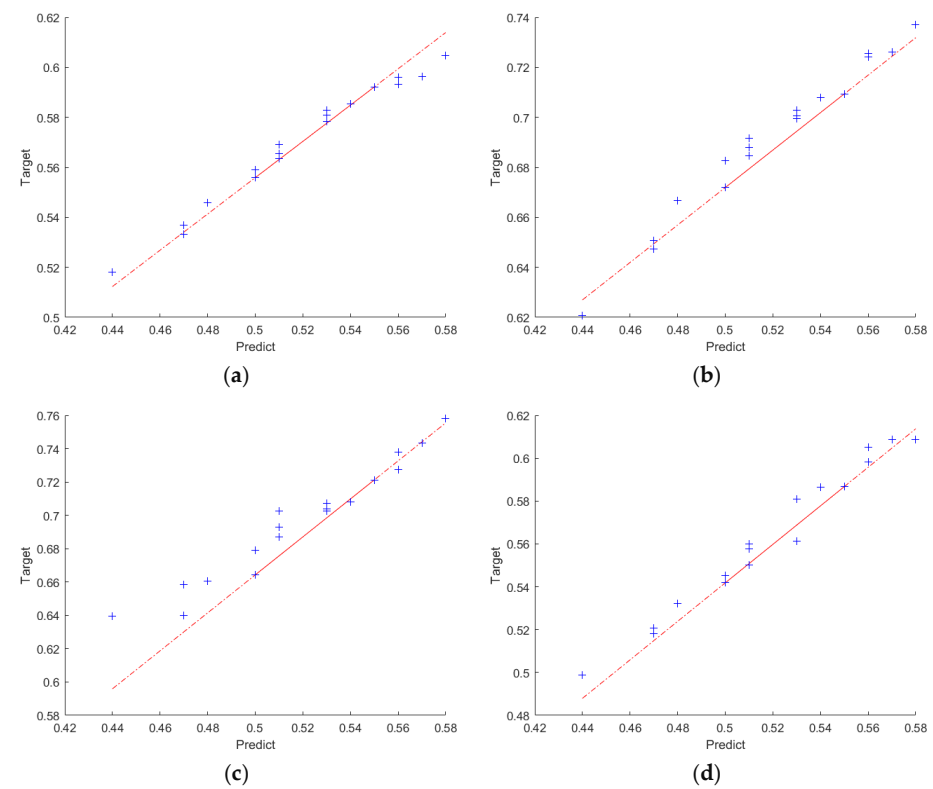


**Figure 9.** Quantile–quantile (QQ) plot between the coefficient of friction and its predicted value obtained by the algorithms. (a). GJO. (b). SOS. (c). GWA. (d). SSA.

## 5. Conclusions

This paper presented a novel machine learning model (LSTM-GJO) that employs a long short-term memory (LSTM) neural network model with golden jackal optimization (GJO) to predict the tribological properties of Cu–Al<sub>2</sub>O<sub>3</sub> nanocomposites with different Al<sub>2</sub>O<sub>3</sub> content and was tested at different wear conditions, applied loads, and sliding speeds. To this purpose, the Cu-based matrix was reinforced with Ag-coated Al<sub>2</sub>O<sub>3</sub> nanoparticles using the ball milling technique. The produced powders were consolidated and sintered to form bulk rounded-shape samples. The produced composite with 10% Al<sub>2</sub>O<sub>3</sub> content showed enhanced microhardness, reaching 165 HV compared to the 63.9 HV of pure Cu. Despite this large Al<sub>2</sub>O<sub>3</sub> content, the microstructure of the composite was homogenous, which contributed to the mechanical properties' enchantment. Moreover, the grain refinement caused by the presence of the Al<sub>2</sub>O<sub>3</sub> nanoparticles in the Cu microstructure helped with hardness improvement. The wear rate was reduced with increasing Al<sub>2</sub>O<sub>3</sub> concentration due to the lower deformation of the pin during the sliding over the disk caused by the reduced plasticity of the composites. Moreover, the coefficient friction was decreased due to the lower contact area between the composites and the disk. Due to the large number of parameters during the wear test that include the reinforcement content, sliding speed, and load, the machine learning model was developed and used to predict the wear rates in a simple and fast process. This developed LSTM-GJO depends on enhancing the performance of the LSTM neural network model using a GJO optimizer. To validate the performance of the developed LSTM-GJO model, a set of real-world data collected from Cu–Al<sub>2</sub>O<sub>3</sub> nanocomposites was used. In addition, the results of the LSTM-GJO were compared with other models, SCA and GWO and SSA. The experimental results showed the overall superiority of LSTM-GJO among the compared algorithms.

**Author Contributions:** I.R.N. (project administration, funding acquisition, data curation); A.M.S. (software, validation, formal analysis, investigation); A.F. (formal analysis, investigation); A.W.A. (software, visualization, data curation); M.A.E. (conceptualization, methodology, formal analysis); M.E. (conceptualization, methodology, review and editing). All authors have read and agreed to the published version of the manuscript.

**Funding:** This project was funded by the Deanship of Scientific Research (DSR) at King Abdulaziz University, Jeddah, under grant no. G: 59-135-1442. The authors, therefore, acknowledge with thanks the DSR for its technical and financial support.

**Data Availability Statement:** Not applicable.

**Conflicts of Interest:** The authors declare no conflict of interest.

## References

1. Zhan, Y.Z.; Shi, X.B.; Xie, H.F. Microstructural investigation on antifriction characteristics of self-lubricating copper hybrid composite. *Mater. Sci. Technol.* **2006**, *22*, 368–374. [[CrossRef](#)]
2. Akbarpour, M.; Alipour, S. Wear and friction properties of spark plasma sintered SiC/Cu nanocomposites. *Ceram. Int.* **2017**, *43*, 13364–13370. [[CrossRef](#)]
3. Li, J.; Mayer, J.W. Colgan EG: Oxidation protection in copper copper alloy thin films. *J. Appl. Phys.* **1991**, *70*, 2820–2827.
4. Smirnov, V.M.; Shalunov, E.P.; Golyushov, I.S. Physical and mechanical properties and structure of copper-based composite materials for diamond tools binder. *J. Phys. Conf. Ser.* **2020**, *1431*, 012054. [[CrossRef](#)]
5. Nicolicescu, C.; Nicoară, V.H.; Bălulescu, C.S. Synthesis of Cu/Cr and Cu/Cr/W Materials by Powder Metallurgy Techniques. *Appl. Mech. Mater.* **2018**, *880*, 241–247. [[CrossRef](#)]
6. Zhang, J.; Huang, Y.; Liu, Y.; Wang, Z. Direct diffusion bonding of immiscible tungsten and copper at temperature close to Copper's melting point. *Mater. Des.* **2018**, *137*, 473–480. [[CrossRef](#)]
7. Sun, X.; Ebrahimi, M.; Attarilar, S. The decisive impact of microstructure on the machinability of pure copper. *Arch. Civ. Mech. Eng.* **2021**, *21*, 136. [[CrossRef](#)]
8. Han, S.Z.; Kim, K.H.; Kang, J.; Joh, H.; Kim, S.M.; Ahn, J.H.; Lee, J.; Lim, S.H.; Han, B. Design of exceptionally strong and conductive Cu alloys beyond the conventional speculation via the interfacial energy-controlled dispersion of  $\gamma$ -Al<sub>2</sub>O<sub>3</sub> nanoparticles. *Sci. Rep.* **2015**, *5*, 17364.
9. Hussain, M.Z.; Khan, S.; Sarmah, P. Optimization of powder metallurgy processing parameters of Al<sub>2</sub>O<sub>3</sub>/Cu composite through Taguchi method with Grey relational analysis. *J. King Saud. Univ.-Eng. Sci.* **2020**, *32*, 274.

10. Güler, O.; Varol, T.; Alver, Ü.; Kaya, G.; Yıldız, F. Microstructure and wear characterization of Al<sub>2</sub>O<sub>3</sub> reinforced silver coated copper matrix composites by electroless plating and hot pressing methods. *Mater. Today Commun.* **2021**, *27*, 102205. [[CrossRef](#)]
11. Jamaati, R.; Toroghinejad, M.R. Application of ARB process for manufacturing high-strength, finely dispersed and highly uniform Cu/Al<sub>2</sub>O<sub>3</sub> composite. *Mater. Sci. Eng. A* **2010**, *527*, 7430–7435. [[CrossRef](#)]
12. Shehata, F.; Fathy, A.; Abdelhameed, M.; Moustafa, S. Fabrication of copper–alumina nanocomposites by mechano-chemical routes. *J. Alloy. Compd.* **2009**, *476*, 300–305. [[CrossRef](#)]
13. Wagih, A.; Fathy, A. Experimental investigation and FE simulation of spherical indentation on nano-alumina reinforced copper matrix composite produced by three different techniques. *Adv. Powder Technol.* **2017**, *28*, 1954. [[CrossRef](#)]
14. Shehata, F.; Fathy, A.; Abdelhameed, M.; Moustafa, S. Preparation and properties of Al<sub>2</sub>O<sub>3</sub> nanoparticle reinforced copper matrix composites by in situ processing. *Mater. Des.* **2009**, *30*, 2756–2762. [[CrossRef](#)]
15. Fathy, A.; Megahed, A.A. Prediction of abrasive wear rate of in situ Cu–Al<sub>2</sub>O<sub>3</sub> nanocomposite using artificial neural networks. *Int. J. Adv. Manuf. Technol.* **2012**, *62*, 953–963. [[CrossRef](#)]
16. Shao, G.; Liu, P.; Zhang, K.; Li, W.; Chen, X.; Ma, F. Mechanical properties of graphene nanoplates reinforced copper matrix composites prepared by electrostatic self-assembly and spark plasma sintering. *Mater. Sci. Eng. A* **2019**, *739*, 329–334. [[CrossRef](#)]
17. Sadoun, A.; Fathy, A. Experimental study on tribological properties of Cu–Al<sub>2</sub>O<sub>3</sub> nanocomposite hybridized by graphene nanoplatelets. *Ceram. Int.* **2019**, *45*, 24784–24792. [[CrossRef](#)]
18. Wagih, A.; Fathy, A. Improving compressibility and thermal properties of Al–Al<sub>2</sub>O<sub>3</sub> nanocomposites using Mg particles. *J. Mater. Sci.* **2018**, *53*, 11393–11402. [[CrossRef](#)]
19. Fathy, A.; Abu-Oqail, A.; Wagih, A. Improved mechanical and wear properties of hybrid Al–Al<sub>2</sub>O<sub>3</sub>/GNPs electro-less coated Ni nanocomposite. *Ceram. Int.* **2018**, *44*, 22135–22145. [[CrossRef](#)]
20. Wagih, A.; Abu-Oqail, A.; Fathy, A.Y. Effect of GNPs content on thermal and mechanical properties of a novel hybrid Cu–Al<sub>2</sub>O<sub>3</sub>/GNPs coated Ag nanocomposite. *Ceram. Int.* **2019**, *45*, 1115. [[CrossRef](#)]
21. Abu-Oqail, A.; Samir, A.; Essa, A.; Wagih, A.; Fathy, A. Effect of GNPs coated Ag on microstructure and mechanical properties of Cu–Fe dual-matrix nanocomposite. *J. Alloy. Compd.* **2019**, *781*, 64–74. [[CrossRef](#)]
22. Fathy, A.; Ibrahim, D.; Elkady, O.; Hassan, M. Evaluation of mechanical properties of 1050–Al reinforced with SiC particles via accumulative roll bonding process. *J. Compos. Mater.* **2018**, *53*, 209–218. [[CrossRef](#)]
23. Tjong, S.C.; Lau, K.C. Tribological behavior of SiC particle-reinforced copper matrix composites. *Mater. Lett.* **2000**, *43*, 274–280. [[CrossRef](#)]
24. Fathy, A.; Elkady, O.; Abu-Oqail, A. Synthesis and characterization of Cu–ZrO<sub>2</sub> nanocomposite produced by thermochemical process. *J. Alloy. Compd.* **2017**, *719*, 411–419. [[CrossRef](#)]
25. Fathy, A.; Wagih, A.; El-Hamid, M.A.; Hassan, A. Effect of mechanical milling on the morphology and structural evaluation of Al–Al<sub>2</sub>O<sub>3</sub> nanocomposite powders. *Int. J. Eng. Trans. A Basics* **2013**, *27*, 625.
26. Fathy, A.; Elkady, O.; Abu-Oqail, A. Microstructure, mechanical and wear properties of Cu–ZrO<sub>2</sub> nanocomposites. *Mater. Sci. Technol.* **2017**, *3*, 2138. [[CrossRef](#)]
27. Fathy, A. Investigation on microstructure and properties of Cu–ZrO<sub>2</sub> nanocomposites synthesized by in situ processing. *Mater. Lett.* **2018**, *213*, 95. [[CrossRef](#)]
28. El-Wazery, M.S.; El-Desouky, A.R.; Hamed, O.A.; Fathy, A.; Mansour, N.A. Electrical and mechanical performance of zirconium-nickel functionally graded materials. *Int. J. Eng. Trans. A Basics* **2013**, *26*, 375–382.
29. Chen, X.; Bao, R.; Yi, J.; Fang, D.; Tao, J.; Liu, Y. Enhancing Interfacial Bonding and Tensile Strength in CNT–Cu Composites by a Synergetic Method of Spraying Pyrolysis and Flake Powder Metallurgy. *Materials* **2019**, *12*, 670. [[CrossRef](#)]
30. Ghorbani, A.; Sheibani, S.; Ataie, A. Microstructure and mechanical properties of consolidated Cu–Cr–CNT nanocomposite prepared via powder metallurgy. *J. Alloy. Compd.* **2018**, *732*, 818–827. [[CrossRef](#)]
31. Güler, O.; Alver, Ü.; Varol, T. Fabrication and characterization of novel layered materials produced by electroless plating and hot pressing. *J. Alloy. Compd.* **2020**, *835*, 155278. [[CrossRef](#)]
32. Feng, J.; Liang, S.; Guo, X.; Zhang, Y.; Song, K. Electrical conductivity anisotropy of copper matrix composites reinforced with SiC whiskers. *Nanotechnol. Rev.* **2019**, *8*, 285–292. [[CrossRef](#)]
33. Jamwal, A.; Mittal, P.; Agrawal, R.; Gupta, S.; Kumar, D.; Sadasivuni, K.K.; Gupta, P. Towards sustainable copper matrix composites: Manufacturing routes with structural, mechanical, electrical and corrosion behaviour. *J. Compos. Mater.* **2020**, *54*, 2635–2649. [[CrossRef](#)]
34. Güler, O.; Varol, T.; Alver, Ü.; Biyik, S. The wear and arc erosion behavior of novel copper based functionally graded electrical contact materials fabricated by hot pressing assisted electroless plating. *Adv. Powder Technol.* **2021**, *32*, 2873–2890. [[CrossRef](#)]
35. Zhao, Q.; Shao, Z.; Liu, C.; Jiang, M.; Li, X.; Zevenhoven, R.; Saxén, H. Preparation of Cu–Cr alloy powder by mechanical alloying. *J. Alloy. Compd.* **2014**, *607*, 118–124. [[CrossRef](#)]
36. Shkodich, N.; Rogachev, A.; Vadchenko, S.; Moskovskikh, D.; Sachkova, N.; Rouvimov, S.; Mukasyan, A. Bulk Cu–Cr nanocomposites by high-energy ball milling and spark plasma sintering. *J. Alloy. Compd.* **2014**, *617*, 39–46. [[CrossRef](#)]
37. Patra, S.; Gouthama; Mondal, K. Densification behavior of mechanically milled Cu–8at% Cr alloy and its mechanical and electrical properties. *Prog. Nat. Sci.* **2014**, *24*, 608–622. [[CrossRef](#)]
38. Gao, N.; Huttunen-Saarivirta, E.; Tiainen, T.; Hemmilä, M. Influence of prior deformation on the age hardening of a phosphorus-containing Cu–0.61wt.%Cr alloy. *Mater. Sci. Eng. A* **2003**, *342*, 270. [[CrossRef](#)]

39. Yin, Z.; Tao, S.; Zhou, X.; Ding, C. Microstructure and mechanical properties of Al<sub>2</sub>O<sub>3</sub>–Al composite coatings deposited by plasma spraying. *Appl. Surf. Sci.* **2008**, *254*, 1636–1643. [[CrossRef](#)]
40. Wang, Q.; Sun, Q.; Zhang, M.-X.; Niu, W.-J.; Tang, C.-B.; Wang, K.-S.; Rui, X.; Zhai, L.; Wang, L. The influence of cold and detonation thermal spraying processes on the microstructure and properties of Al-based composite coatings on Mg alloy. *Surf. Coat. Technol.* **2018**, *352*, 627–633. [[CrossRef](#)]
41. Wang, Q.; Birbilis, N.; Huang, H.; Zhang, M.-X. Microstructure characterization and nanomechanics of cold-sprayed pure Al and Al–Al<sub>2</sub>O<sub>3</sub> composite coatings. *Surf. Coat. Technol.* **2013**, *232*, 216–223. [[CrossRef](#)]
42. Da Silva, F.S.; Bedoya, J.; Dosta, S.; Cinca, N.; Cano, I.G.; Guilemany, J.M.; Benedetti, A.V. Corrosion characteristics of cold gas spray coatings of reinforced aluminum deposited onto carbon steel. *Corros. Sci.* **2017**, *114*, 57–71. [[CrossRef](#)]
43. Yu, M.; Suo, X.K.; Li, W.Y.; Wang, Y.Y.; Liao, H.L. Microstructure, mechanical property and wear performance of cold sprayed Al<sub>50</sub>Si<sub>50</sub> composite coatings: Effect of reinforcement content. *Appl. Surf. Sci.* **2014**, *289*, 188–196. [[CrossRef](#)]
44. Yandouzi, M.; Böttger, A.J.; Hendriks, R.W., A.; Brochu, M.; Richer, P.; Charest, A.; Jodoin, B. Microstructure and mechanical properties of B<sub>4</sub>C reinforced Al-based matrix composite coatings deposited by CGDS and PGDS processes. *Surf. Coat. Technol.* **2010**, *205*, 2234–2246. [[CrossRef](#)]
45. Fathy, A.; Shehata, F.; Abdelhameed, M.; Elmahdy, M. Compressive and wear resistance of nanometric alumina reinforced copper matrix composites. *Mater. Des.* **2012**, *36*, 100–107. [[CrossRef](#)]
46. Daoush, W.M.; Lim, B.K.; Mo, C.B.; Nam, D.H.; Hong, S.H. Electrical and mechanical properties of carbon nanotube reinforced copper nanocomposites fabricated by electroless deposition process. *Mater. Sci. Eng. A* **2009**, *513–514*, 247–253. [[CrossRef](#)]
47. Sadoun, A.M.; Fathy, A.; Abu-Oqail, A.; Elmetwaly, H.T.; Wagih, A. Structural, mechanical and tribological properties of Cu–ZrO<sub>2</sub>/GNPs hybrid nanocomposites. *Ceram. Int.* **2020**, *46*, 7586–7594. [[CrossRef](#)]
48. Shukla, S.; Seal, S.; Rahaman, Z.; Scammon, K. Electroless copper coating of cenospheres using silver nitrate activator. *Mater. Lett.* **2002**, *57*, 151–156. [[CrossRef](#)]
49. Barakat, W.; Wagih, A.; Elkady, O.A.; Abuqail, A.; Fathy, A.; El-Nikhaily, A. Effect of Al<sub>2</sub>O<sub>3</sub> nanoparticles content and compaction temperature on properties of Al–Al<sub>2</sub>O<sub>3</sub> coated Cu nanocomposites. *Compos. Part B Eng.* **2019**, *175*, 107140. [[CrossRef](#)]
50. Khatir, S.; Boutchicha, D.; Le Thanh, C.; Tran-Ngoc, H.; Nguyen, T.; Abdel-Wahab, M. Improved ANN technique combined with Jaya algorithm for crack identification in plates using XIGA and experimental analysis. *Theor. Appl. Fract. Mech.* **2020**, *107*, 102554. [[CrossRef](#)]
51. Zenzen, R.; Khatir, S.; Belaidi, I.; Le Thanh, C.; Wahab, M.A. A modified transmissibility indicator and Artificial Neural Network for damage identification and quantification in laminated composite structures. *Compos. Struct.* **2020**, *248*, 112497. [[CrossRef](#)]
52. Wang, S.; Wang, H.; Zhou, Y.; Liu, J.; Dai, P.; Du, X.; Wahab, M.A. Automatic laser profile recognition and fast tracking for structured light measurement using deep learning and template matching. *Measurement* **2021**, *169*, 108362. [[CrossRef](#)]
53. Zhao, W.; Wang, L.; Mirjalili, S. Artificial hummingbird algorithm: A new bio-inspired optimizer with its engineering applications. *Comput. Methods Appl. Mech. Eng.* **2021**, *388*, 114194. [[CrossRef](#)]
54. Hasheminejad, N.; Pipintakos, G.; Vuyc, C.; De Kerf, T.; Ghalandari, T.; Blom, J.; Bergh, W.V.D. Utilizing deep learning and advanced image processing techniques to investigate the microstructure of a waxy bitumen. *Constr. Build. Mater.* **2021**, *313*, 125481. [[CrossRef](#)]
55. Sadoun, A.; Najjar, I.; Fathy, A.; Elaziz, M.A.; Al-Qaness, M.A.; Abdallah, A.; Elmahdy, M. An enhanced Dendritic Neural Algorithm to predict the wear behavior of alumina coated silver reinforced copper nanocomposites. *Alex. Eng. J.* **2022**. [[CrossRef](#)]
56. Dobbelaere, M.R.; Plehiers, P.P.; Van de Vijver, R.; Stevens, C.V.; Van Geem, K.M. Machine learning in chemical engineering: Strengths, weaknesses, opportunities, and threats. *Engineering* **2021**, *7*, 1201–1211. [[CrossRef](#)]
57. Zhong, S.; Zhang, K.; Bagheri, M.; Burken, J.G.; Gu, A.; Li, B.; Ma, X.; Marrone, B.L.; Ren, Z.J.; Schrier, J.; et al. Machine learning: New ideas and tools in environmental science and engineering. *Environ. Sci. Technol.* **2021**, *55*, 12741–12754. [[CrossRef](#)]
58. Sadoun, A.M.; Najjar, I.R.; Alsuruji, G.S.; Wagih, A.; Elaziz, M.A. Utilizing a Long Short-Term Memory Algorithm Modified by Dwarf Mongoose Optimization to Predict Thermal Expansion of Cu–Al<sub>2</sub>O<sub>3</sub> Nanocomposites. *Mathematics* **2022**, *10*, 1050. [[CrossRef](#)]
59. Najjar, I.; Sadoun, A.; Alsuruji, G.S.; Elaziz, M.A.; Wagih, A. Predicting the mechanical properties of Cu–Al<sub>2</sub>O<sub>3</sub> nanocomposites using machine learning and finite element simulation of indentation experiments. *Ceram. Int.* **2022**, *48*, 7748–7758. [[CrossRef](#)]
60. Haimed, A.M.A.; Saba, T.; Albasha, A.; Rehman, A.; Kolivand, M. Viral reverse engineering using Artificial Intelligence and big data COVID-19 infection with Long Short-term Memory (LSTM). *Environ. Technol. Innov.* **2021**, *22*, 101531. [[CrossRef](#)]
61. Xiaoyun, Q.; Xiaoning, K.; Chao, Z.; Shuai, J.; Xiuda, M. Short-term prediction of wind power based on deep long short-term memory. In Proceedings of the 2016 IEEE PES Asia-Pacific Power and Energy Engineering Conference (APPEEC), Xi'an, China, 25–28 October 2016; IEEE: Piscataway, NJ, USA, 2016; pp. 1148–1152.
62. Bilgili, M.; Arslan, N.; Şekertekin, A.; Yaşar, A. Application of long short-term memory (LSTM) neural network based on deeplearning for electricity energy consumption forecasting. *Turk. J. Electr. Eng. Comput. Sci.* **2022**, *30*, 140–157.
63. Liu, W.; Pan, J.; Ren, Y.; Wu, Z.; Wang, J. Coupling prediction model for long-term displacements of arch dams based on long short-term memory network. *Struct. Control Health Monit.* **2020**, *27*, e2548. [[CrossRef](#)]
64. Chopra, N.; Ansari, M.M. Golden jackal optimization: A novel nature-inspired optimizer for engineering applications. *Expert Syst. Appl.* **2022**, *198*, 116924. [[CrossRef](#)]
65. Dong, L.L.; Ahangarkani, M.; Chen, W.G.; Zhang, Y.S. Recent progress in development of tungsten-copper composites: Fabrication, modification and applications. *Int. J. Refract. Met. Hard Mater.* **2018**, *75*, 30–42. [[CrossRef](#)]

66. Santos, T.D.E.D.S.; Regiani, I.; Rocha, R.J.; Rocco, J. Copper/Iron Brake Friction for Military Aircraft Application. *J. Aerosp. Technol. Manag.* **2018**, *10*. [[CrossRef](#)]
67. Le, X.H.; Ho, H.V.; Lee, G.; Jung, S. Application of Long Short-Term Memory (LSTM) Neural Network for Flood Forecasting. *Water* **2019**, *11*, 1387. [[CrossRef](#)]
68. Wagih, A. Mechanical properties of Al–Mg/Al<sub>2</sub>O<sub>3</sub> nanocomposite powder produced by mechanical alloying. *Adv. Powder Technol.* **2015**, *26*, 253–258. [[CrossRef](#)]
69. Khamaj, A.; Farouk, W.M.; Shewakh, W.M.; Abu-Oqail AM, I.; Wagih, A.; Abu-Okail, M. Effect of lattice structure evolution on the thermal and mechanical properties of Cu–Al<sub>2</sub>O<sub>3</sub>/GNPs nanocomposites. *Ceram. Int.* **2021**, *47*, 16511–16520. [[CrossRef](#)]
70. Sadoun, A.M.; Najjar IM, R.; Wagih, A. Electroless-plating of Ag nanoparticles on Al<sub>2</sub>O<sub>3</sub> and graphene Nano sheets (GNs) for improved wettability and properties of Al–Al<sub>2</sub>O<sub>3</sub>/GNs nanocomposites. *Ceram. Int.* **2021**, *47*, 10855–10865. [[CrossRef](#)]
71. Sadoun, A.M.; Meselhy, A.F.; Abdallah, A.W. Microstructural, mechanical and wear behavior of electroless assisted silver coated Al<sub>2</sub>O<sub>3</sub>–Cu nanocomposites. *Mater. Chem. Phys.* **2021**, *266*, 124562. [[CrossRef](#)]
72. Shaat, M.; Fathy, A.; Wagih, A. Correlation between grain boundary evolution and mechanical properties of ul-trafine-grained metals. *Mech. Mater.* **2020**, *143*, 103321. [[CrossRef](#)]
73. Abd-Elwahed, M.; Wagih, A.; Najjar, I. Correlation between micro/nano-structure, mechanical and tribological properties of copper-zirconia nanocomposites. *Ceram. Int.* **2019**, *46*, 56–65. [[CrossRef](#)]
74. Cheng, M.-Y.; Prayogo, D. Symbiotic Organisms Search: A new metaheuristic optimization algorithm. *Comput. Struct.* **2014**, *139*, 98–112. [[CrossRef](#)]
75. Ibrahim, R.A.; Abd Elaziz, M.; Lu, S. Chaotic opposition-based grey-wolf optimization algorithm based on differ-ential evolution and disruption operator for global optimization. *Expert Syst. Appl.* **2018**, *108*, 1–27. [[CrossRef](#)]
76. Mirjalili, S.; Gandomi, A.H.; Mirjalili, S.Z.; Saremi, S.; Faris, H.; Mirjalili, S.M. Salp Swarm Algorithm: A bio-inspired optimizer for engineering design problems. *Adv. Eng. Softw.* **2017**, *114*, 163–191. [[CrossRef](#)]